ELSEVIER

*Composite Structures* **28** (1994) 357–373

0263-8223/94/$7.00

# Free edge delamination in carbon–epoxy laminates: a novel numerical/experimental approach

**J. C. J. Schellekens* & R. De Borst‡**
*Department of Civil Engineering, Delft University of Technology, PO Box 5048, 2600 GA Delft, The Netherlands*

A geometrically and physically nonlinear finite element approach is presented for the analysis of mode-I and mixed-mode free edge delamination in composite laminates which properly accounts for the effects of initial thermal and hygroscopic stresses. A constitutive model based on nonlinear fracture mechanics is used to describe delamination. An orthotropic softening plasticity model is used to determine the initiation and propagation of delamination. Although the orthotropic yield surface is based on stresses, it is proved, that, in combination with a softening type of post-failure response controlled by the fracture toughness, the approach results in a unique and physically realistic solution upon mesh refinement. The results from the nonlinear finite element computations, including predictive analysis, are compared with mode-I and mixed-mode free edge delamination experiments. This comparison shows that the numerical results are within 10% of the experimental data.

## 1 INTRODUCTION

Due to the varying fibre orientations and the ensuing anisotropy of a composite material, each ply of a laminate behaves independently of the other plies. Large edge stresses are then necessary to preserve compatibility of deformations. Together with matrix cracks these transverse stresses near the free edge are primarily responsible for the initiation of this type of delamination. To gain more insight into the complex phenomenon of delamination, we need procedures that give us accurate predictions of delamination onset and growth. In this contribution we shall focus on free edge delamination in uniaxially loaded laminates (Fig. 1). which has been the subject of much research since the early 1970s.[1–12]

Although a finite element analysis combined with stress-based or strain-based fracture criteria like the one proposed by Tsai and Wu[13] is often used to predict the failure of a composite structure, it is widely recognised that the results of such a procedure should be regarded with caution because they strongly depend upon the finite element discretisation. To avoid this problem of mesh dependence Kim and Soni[4] have used an average stress criterion. The introduction of the ply thickness as a length scale, which basically is a first step towards so-called non-local models,[14] is essential in their approach. However, delamination not necessarily progresses at the location where the stresses have the maximum values, but grows at the interface where the energy release rate exceeds the fracture toughness of the material. This casts doubt on failure predictions that are purely based on stress or strain criteria.

In view of the above arguments a crack-extension or crack-closure method seems more appropriate in delamination analysis.[5–9,11,15] Since these linear elastic fracture mechanics procedures calculate the energy release rate from nodal forces and displacements rather than from stresses and strains, the results are mesh independent, although a certain level of mesh refinement is necessary. A disadvantage of these linear fracture mechanics options is that, before we can determine the interface that is the most critical, the energy release rate has to be calculated at each

*On leave from the Institute for Statics and Dynamics of Aerospace Structures, University of Stuttgart, Stuttgart, Germany.
‡Also at Department of Mechanical Engineering, Eindhoven University of Technology.

location where delamination may initiate. This can become an expensive exercise, especially for large structures.

In this contribution a procedure is presented for the prediction of delamination onset and growth in axially loaded graphite–epoxy laminates. The plies of the laminate are modelled by generalised plane-strain elements with cubic interpolations (Section 2.1), which are connected by cubic line interface elements which have the ability to model the geometric discontinuity that arises during the delamination process (Fig. 2). As will be outlined in Section 2.2, these interface elements have initially a zero thickness with four pairs of overlapping nodes. After initiation of delamination, that is, when the elastic limit of the interface elements is exceeded, the nodes of a pair are gradually released and an internal traction-free boundary is created. In the present approach initiation appears once an orthotropic yield condition is violated.[16,17] Since this criterion is purely based on stresses, the initiation of delamination suffers to a certain extent from mesh sensitivity, that is, for smaller elements the high stress gradients are captured more accurately. High peak stresses are computed, which for a lower level of loading cause violation of the stress-based delamination initiation criterion. The situation is different with respect to delamination propagation. The stress–strain behaviour after the onset of delamination is governed by a softening type of response, i.e. a degradation of strength and stiffness of the interface with increasing inelastic deformations. This implies a negative slope in the stress–strain diagram. The quintessence of our approach is that the surface under the softening

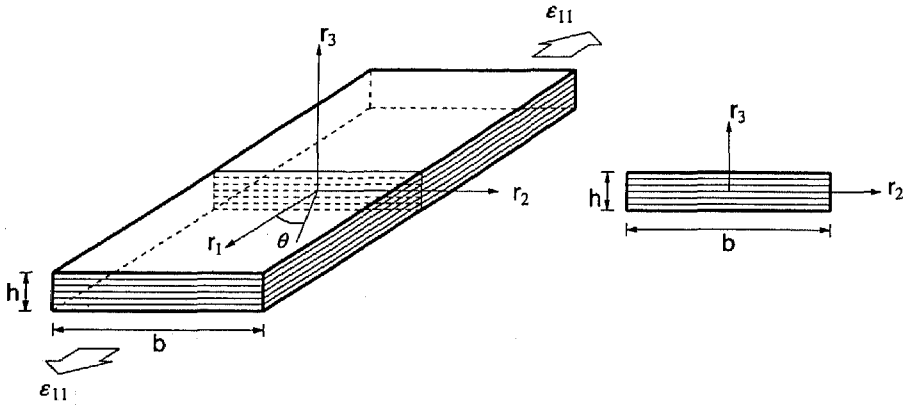


**Fig. 1.** A free edge delamination specimen subjected to a uniaxial strain.

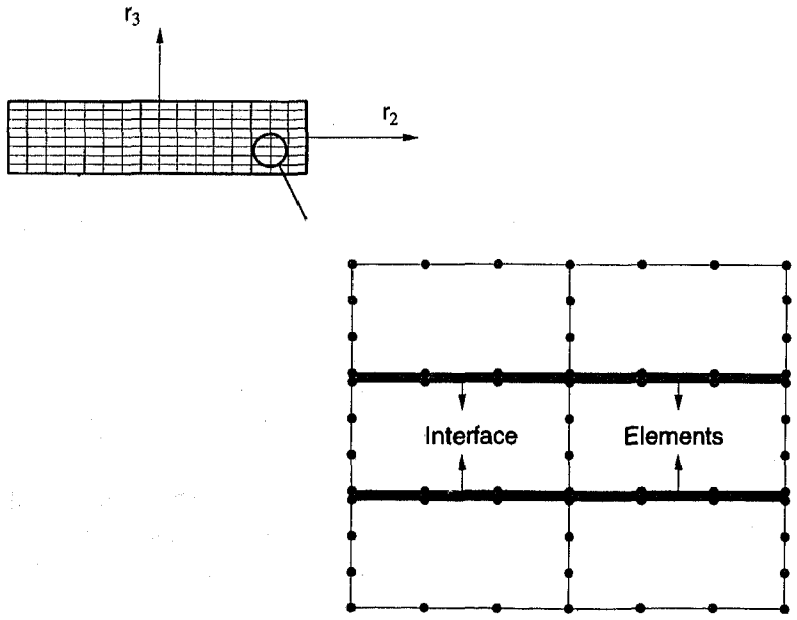


**Fig. 2.** A cubic interface element.

curve is equal to the critical energy release rate (fracture toughness) $G_c$ of the ply interface that delaminates. This ensures on the one hand a correct energy release during delamination propagation, so that propagation is independent of the mesh refinement, and on the other hand it results in a proper description of the size effect, i.e. a thicker laminate fails at a lower ultimate strain (more brittle).

The performance of the method will be demonstrated by means of the analyses of free edge delamination in different graphite–epoxy specimens under uniaxial tension (Sections 4 and 5). In the analyses the emphasis is put on the effects on the ultimate load capacity of the laminate thickness (size effect), mesh refinement and of the initial thermal stresses. A part of the simulations of mode-I and mixed-mode delamination has been compared with experiments reported by Wang *et al.*[5,1] and O'Brien.[6,7] However, due to the fact that not all essential parameters necessary for our approach were available in the literature, a limited experimental programme was carried out. The values for the delamination onset strain obtained in the experiments have been predicted by numerical analyses.

Since standard arc-length control methods[18–20] did not lead to a converged solution, the nonlinear analyses have been carried out under indirect displacement control, a solution procedure which is described in Refs 15, 16, 21 and 22. Using this numerical technique the increment of the applied out-of-plane axial strain (Fig. 1) within a loading step is determined by the requirement that sum of the Crack Opening Displacements of the ply interface where delamination occurs has a constant value during each iteration in a loading step. The occurrence of a negative pivot has been used as a criterion for a sign-reversal of the load increment.

The effects of matrix-cracking have been neglected in the analyses. So the ply material is assumed to remain elastic.

## 2 ELEMENT FORMULATIONS

### 2.1 Generalised plane-strain elements

In free edge delamination testing specimens are subjected to a uniaxial tensile or compressive load in the $r_1$-direction (Fig. 1). Since the length of the laminates used in these experiments is large when compared to their width and thickness it can be assumed that, at a certain distance from the ends of the specimen, the in-plane displacements in the $r_2r_3$-plane are independent of the $r_1$-coordinate. For the displacement field of a cross-section at a certain distance from the ends where the load is introduced, this results in the following set of equations for the displacement field $u(u_1, u_2, u_3)$,[1,2,6,10]

$$\begin{aligned} u_1(r_1, r_2, r_3) &= \mu\varepsilon_{11} r_1 + u_1(r_2, r_3) \\ u_2(r_1, r_2, r_3) &= u_2(r_2, r_3) \\ u_3(r_1, r_2, r_3) &= u_3(r_2, r_3) \end{aligned} \tag{1}$$

with $\varepsilon_{11}$ a normalised strain that is prescribed in the $r_1$-direction of the specimen and $\mu$ is a parameter that scales the applied strain load. This displacement field corresponds to a so-called generalised plane-strain state in which there exists a constant (non-zero) strain in the direction normal to the element plane ($r_1$). Equation (1) also shows that in contrast to regular two-dimensional elements, generalised plane-strain elements have three translational degrees of freedom per node, which enables one to model the warping of a cross-section.

With the increment of the Green–Lagrange strain tensor given by

$$\Delta\gamma_{ij} = \frac{1}{2}\left(\frac{\partial\Delta u_i}{\partial r_j} + \frac{\partial\Delta u_j}{\partial r_i} + \frac{\partial u_k}{\partial r_i}\frac{\partial\Delta u_k}{\partial r_j} + \frac{\partial\Delta u_k}{\partial r_i}\frac{\partial u_k}{\partial r_j} + \frac{\partial\Delta u_k}{\partial r_i}\frac{\partial\Delta u_k}{\partial r_j}\right) \tag{2}$$

and noting that, for generalised plane-strain conditions, $\Delta u_{1,r_1} = \Delta\mu\varepsilon_{11}, \Delta u_{2,r_1} = 0$ and $\Delta u_{3,r_1} = 0$ we obtain for the strain increment $\Delta\gamma$:

$$\Delta\gamma = \Delta g + \Delta\varepsilon + \Delta\eta + \Delta\mu\varepsilon_l \tag{3}$$

where $\Delta \mathbf{g}$ is of the order zero in the displacement increments $\Delta u_k$,

$$\Delta \mathbf{g} = \begin{pmatrix} (F_{11}-1)\Delta\mu\varepsilon_{11} + 1/2\Delta\mu^2\varepsilon_{11}^2 \\ 0 \\ 0 \\ F_{12}\Delta\mu\varepsilon_{11} \\ 0 \\ F_{13}\Delta\mu\varepsilon_{11} \end{pmatrix} \tag{4}$$

and $\Delta\boldsymbol{\varepsilon}$ and $\Delta\boldsymbol{\eta}$ are linear and quadratic in the displacement increments, respectively:

$$\Delta\boldsymbol{\varepsilon} = \begin{pmatrix} 0 \\ F_{12}\Delta u_{1,r_2} + F_{22}\Delta u_{2,r_2} + F_{32}\Delta u_{3,r_2} \\ F_{13}\Delta u_{1,r_3} + F_{23}\Delta u_{2,r_3} + F_{33}\Delta u_{3,r_3} \\ (F_{11} + \Delta\mu\varepsilon_{11})\Delta u_{1,r_2} \\ F_{12}\Delta u_{1,r_3} + F_{13}\Delta u_{1,r_2} + F_{22}\Delta u_{2,r_3} + F_{23}\Delta u_{2,r_2} + F_{32}\Delta u_{3,r_3} + F_{33}\Delta u_{3,r_2} \\ (F_{11} + \Delta\mu\varepsilon_{11})\Delta u_{1,r_3} \end{pmatrix} \tag{5}$$

where the terms $F_{ij}$ designate the components of the deformation gradient ($F_{ij} = \delta_{ij} + \partial u_i/\partial r_j$), and

$$\Delta\boldsymbol{\eta} = \begin{pmatrix} 0 \\ 1/2((\Delta u_{1,r_2})^2 + (\Delta u_{2,r_2})^2 + (\Delta u_{3,r_2})^2) \\ 1/2((\Delta u_{1,r_3})^2 + (\Delta u_{2,r_3})^2 + (\Delta u_{3,r_3})^2) \\ 0 \\ \Delta u_{1,r_2}\Delta u_{1,r_3} + \Delta u_{2,r_2}\Delta u_{2,r_3} + \Delta u_{3,r_2}\Delta u_{3,r_3} \\ 0 \end{pmatrix} \tag{6}$$

In eqn (3) the contribution $\boldsymbol{\varepsilon}_l$ is due to the applied axial strain loading normal to the element plane and reads,

$$\boldsymbol{\varepsilon}_l^{\mathrm{T}} = (\varepsilon_{11}, 0, 0, 0, 0, 0) \tag{7}$$

Extension of eqn (3) to include the effect of moisture and initial thermal strains gives us

$$\Delta\boldsymbol{\gamma} = \Delta\mathbf{g} + \Delta\boldsymbol{\varepsilon} + \Delta\boldsymbol{\eta} + \Delta\mu\boldsymbol{\varepsilon}_l + \Delta T_i\boldsymbol{\alpha} + \Delta C_i\boldsymbol{\beta} \tag{8}$$

with $\Delta T_i$ and $\Delta C_i$ the incremental changes in temperature and moisture content in the current loading step $i$. The vectors $\boldsymbol{\alpha}$ and $\boldsymbol{\beta}$ contain the thermal and hygroscopic expansion coefficients, respectively. Hence, generalised plane-strain elements are not loaded by prescribed displacements or prescribed nodal forces, but by hygro-thermal and out-of-plane surface strains. Assuming that there are no other non-

linear effects in the plies (matrix-cracking, fibre breaking) the stress increment at iteration $j$ is then given by

$$\Delta\boldsymbol{\sigma}_j = \mathbf{D}_P(\Delta\mathbf{g}_j + \Delta\boldsymbol{\varepsilon}_j + \Delta\boldsymbol{\eta}_j + \Delta\mu_j\boldsymbol{\varepsilon}_l + \Delta T_i\boldsymbol{\alpha} + \Delta C_i\boldsymbol{\beta}) \tag{9}$$

with $D_P$ the elastic stress–strain matrix for the plies and $\Delta\mu_j$ the value of the incremental load parameter at iteration $j$. Subtracting the relation for the stresses at the end of the previous iteration $j-1$ from the stresses at the end of the current iteration $j$ results in

$$\boldsymbol{\sigma}_j = \boldsymbol{\sigma}_{j-1} + \mathbf{D}_P(\mathbf{dg}_j + \mathbf{d}\boldsymbol{\varepsilon}_j + \mathbf{d}\boldsymbol{\eta}_j + d\mu_j\boldsymbol{\varepsilon}_l) \tag{10}$$

The $d$-symbol denotes the iterative change of a scalar or vector quantity from iteration $j-1$ to iteration $j$, whereas the $\Delta$-symbol (e.g. eqn (9)) denotes the change of a quantity from the beginning of the current load step to the end of the current iteration.

Because of the absence of external loadings in-plane the equilibrium equation can be written as:

$$\int_{V_0} \delta\boldsymbol{\gamma}_j^{\mathrm{T}}\boldsymbol{\sigma}_j \,\mathrm{d}V_0 = 0 \tag{11}$$

where $\delta$ indicates the variation of a variable. The variation of the Green–Lagrange strain $\delta\boldsymbol{\gamma}_j = \delta\boldsymbol{\gamma}_{j-1} + \delta(\mathbf{d}\boldsymbol{\gamma}_j)$ is given by

$$\delta\boldsymbol{\gamma}_j = \delta(\mathbf{dg}_j) + \delta(\mathbf{d}\boldsymbol{\varepsilon}_j) + \delta(\mathbf{d}\boldsymbol{\eta}_j) \tag{12}$$

since $\Delta T_i$ and $\Delta C_i$ are constant during the loading/time step. We now substitute eqns (10) and (12) in the equilibrium expression (11) and linearise in order to apply Newton's method for the solution of the set of non-linear equations. If we collect the terms that are of the order of zero in the displacement increments at the right hand side we obtain for the virtual work of a body

$$\int_{V_0} \delta(\mathbf{d}\boldsymbol{\varepsilon}_j)^{\mathrm{T}}\mathbf{D}_P\mathbf{d}\boldsymbol{\varepsilon}_j \,\mathrm{d}V_0 + \int_{V_0} \delta(\mathbf{d}\boldsymbol{\eta}_j)^{\mathrm{T}}(\boldsymbol{\sigma}_{j-1} + \mathbf{D}_P\mathbf{dg}_j + d\mu_j\mathbf{D}_P\boldsymbol{\varepsilon}_l) \,\mathrm{d}V_0 = -\int_{V_0} \delta(\mathbf{d}\boldsymbol{\varepsilon}_j)^{\mathrm{T}}(\boldsymbol{\sigma}_{j-1} + \mathbf{D}_P\mathbf{dg}_j + d\mu_j\mathbf{D}_P\boldsymbol{\varepsilon}_l) \,\mathrm{d}V_0 \tag{13}$$

In the remainder of this section we shall elaborate the discretisation of the virtual work eqn (13).

The linear part $\mathbf{d}\boldsymbol{\varepsilon}_j$ of the incremental strain vector is related to the incremental nodal displacement vector $\mathbf{da} = (da_1^1, da_1^2, \ldots, da_1^n, da_2^1, \ldots, da_2^n, da_3^1, \ldots, da_3^n)^{\mathrm{T}}$ through

$$\mathbf{d}\boldsymbol{\varepsilon}_j = \mathbf{B}_L\mathbf{da}_j \tag{14}$$

$\mathbf{B}_L$ denotes the linear strain displacement matrix, which is equal to (cf. eqn (5))

$$\mathbf{B}_L = \begin{bmatrix} \mathbf{0} & \mathbf{0} & \mathbf{0} \\ F_{12}\mathbf{n}_{,r_2} & F_{22}\mathbf{n}_{,r_2} & F_{32}\mathbf{n}_{,r_2} \\ F_{13}\mathbf{n}_{,r_3} & F_{23}\mathbf{n}_{,r_3} & F_{33}\mathbf{n}_{,r_3} \\ (F_{11} + d\mu_j\varepsilon_{11})\mathbf{n}_{,r_2} & \mathbf{0} & \mathbf{0} \\ F_{13}\mathbf{n}_{,r_2} + F_{12}\mathbf{n}_{,r_3} & F_{23}\mathbf{n}_{,r_2} + F_{22}\mathbf{n}_{,r_3} & F_{33}\mathbf{n}_{,r_2} + F_{32}\mathbf{n}_{,r_3} \\ (F_{11} + d\mu_j\varepsilon_{11})\mathbf{n}_{,r_3} & \mathbf{0} & \mathbf{0} \end{bmatrix} \tag{15}$$

where $\mathbf{n}_{,r_i}$ is given by

$$\mathbf{n}_{,r_i} = \left(\frac{\partial N_1}{\partial r_i}, \frac{\partial N_2}{\partial r_i}, \ldots, \frac{\partial N_{nno}}{\partial r_i}\right) \tag{16}$$

with $N_1,\ldots,N_{nno}$ the interpolation polynomials. Using eqn (14) the first term of eqn (13) can be written as

$$\int_{V_0} \delta(\mathbf{d}\boldsymbol{\varepsilon}_j)^{\mathrm{T}}\mathbf{D}_{\mathrm{P}}\mathbf{d}\boldsymbol{\varepsilon}_j \,\mathrm{d}V_0 = \delta(\mathbf{da}_j)^{\mathrm{T}}\int_{V_0} \mathbf{B}_{\mathrm{L}}^{\mathrm{T}}\mathbf{D}_{\mathrm{P}}\mathbf{B}_{\mathrm{L}} \,\mathrm{d}V_0\mathbf{da}_j \tag{17}$$

We next introduce the non-linear strain displacement matrix $\mathbf{B}_{\mathrm{NL}}$

$$\mathbf{B}_{\mathrm{NL}}^{\mathrm{T}} = \begin{bmatrix} 0 & 0 & 0 & \partial_{,r_2} & 0 & 0 & \partial_{,r_3} & 0 & 0 \\ 0 & 0 & 0 & 0 & \partial_{,r_2} & 0 & 0 & \partial_{,r_3} & 0 \\ 0 & 0 & 0 & 0 & 0 & \partial_{,r_2} & 0 & 0 & \partial_{,r_3} \end{bmatrix} \tag{18}$$

with $\partial_{,r_i} = \partial/\partial r_i$. Then, the second term in the left hand of the virtual work expression, which represents the geometric stiffness contribution, becomes

$$\int_{V_0} \delta(\mathbf{d}\boldsymbol{\eta}_j)^{\mathrm{T}}(\boldsymbol{\sigma}_{j-1} + \mathbf{D}_{\mathrm{P}}\mathbf{dg}_j + d\mu_j\mathbf{D}_{\mathrm{P}}\boldsymbol{\varepsilon}_l) \,\mathrm{d}V_0 = \delta(\mathbf{da}_j)^{\mathrm{T}}\int_{V_0} \mathbf{B}_{\mathrm{NL}}^{\mathrm{T}}(\boldsymbol{\Sigma}_{j-1} + \mathbf{E}_j)\mathbf{B}_{\mathrm{NL}} \,\mathrm{d}V_0\mathbf{da}_j \tag{19}$$

where $\boldsymbol{\Sigma}_{j-1}$ is given by

$$\boldsymbol{\Sigma}_{j-1} = \begin{bmatrix} \sigma_{11,j-1}\mathbf{I}_3 & \sigma_{12,j-1}\mathbf{I}_3 & \sigma_{13,j-1}\mathbf{I}_3 \\ \sigma_{21,j-1}\mathbf{I}_3 & \sigma_{22,j-1}\mathbf{I}_3 & \sigma_{23,j-1}\mathbf{I}_3 \\ \sigma_{31,j-1}\mathbf{I}_3 & \sigma_{32,j-1}\mathbf{I}_3 & \sigma_{33,j-1}\mathbf{I}_3 \end{bmatrix} \tag{20}$$

and $\mathbf{E}_j$ reads:

$$\mathbf{E}_j = \begin{bmatrix} \sigma_{g,11}\mathbf{I}_3 & \sigma_{g,12}\mathbf{I}_3 & \sigma_{g,13}\mathbf{I}_3 \\ \sigma_{g,21}\mathbf{I}_3 & \sigma_{g,22}\mathbf{I}_3 & \sigma_{g,23}\mathbf{I}_3 \\ \sigma_{g,31}\mathbf{I}_3 & \sigma_{g,32}\mathbf{I}_3 & \sigma_{g,33}\mathbf{I}_3 \end{bmatrix} \tag{21}$$

with $\sigma_{ij}$ the Second Piola–Kirchhoff stress tensor and $\boldsymbol{\sigma}_{\mathrm{g}}$ given by

$$\boldsymbol{\sigma}_{\mathrm{g}} = \mathbf{D}_{\mathrm{P}}(\mathbf{dg}_j + d\mu_j\boldsymbol{\varepsilon}_l) \tag{22}$$

Substitution of eqns (14), (17) and (19) into eqn (13) and requiring that the virtual work principle holds for any virtual displacement increment yields

$$\mathbf{K}_j\mathbf{da}_j = -\int_{V_0} \mathbf{B}_{\mathrm{L}}^{\mathrm{T}}\boldsymbol{\sigma}_{j-1} \,\mathrm{d}V_0 - d\mu_j\int_{V_0} \mathbf{B}_{\mathrm{L}}^{\mathrm{T}}\mathbf{D}_{\mathrm{P}}\boldsymbol{\varepsilon}_l \,\mathrm{d}V_0 - \int_{V_0} \mathbf{B}_{\mathrm{L}}^{\mathrm{T}}\mathbf{D}_{\mathrm{P}}\mathbf{dg}_j \,\mathrm{d}V_0 \tag{23}$$

where

$$\mathbf{K}_j = \int_{V_0} \mathbf{B}_{\mathrm{L}}^{\mathrm{T}}\mathbf{D}_{\mathrm{P}}\mathbf{B}_{\mathrm{L}} \,\mathrm{d}V_0 + \int_{V_0} \mathbf{B}_{\mathrm{NL}}^{\mathrm{T}}(\boldsymbol{\Sigma} + \mathbf{E})\mathbf{B}_{\mathrm{NL}} \,\mathrm{d}V_0 \tag{24}$$

defines the element tangent stiffness matrix.

### 2.2 Interface elements

The generalised plane strain elements that are used to model the plies of the laminate are connected by interface elements (see Figs 2 and 3).[15–17,22–26] Although Figs 2 and 3 do not show it explicitly, initially the nodes of the upper and lower side of the element are located at the same position. In the elastic stage of the calculation no additional deformations are allowed in the finite element model because of the introduction of the interface elements in the finite element model. Therefore a sufficiently high dummy

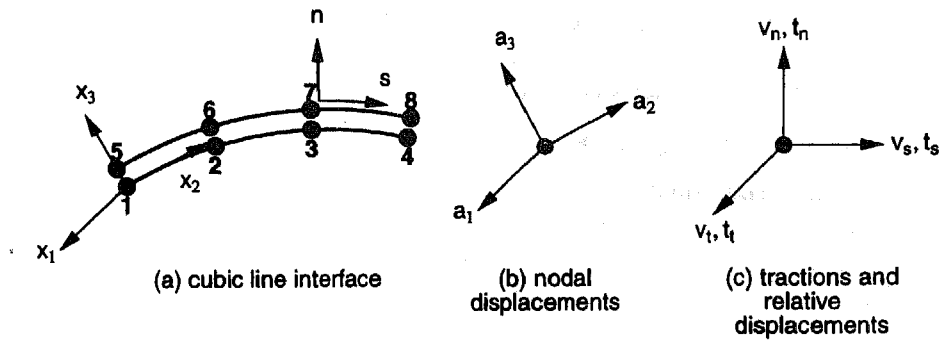


**Fig. 3.** Continuum elements connected by line interface elements. Initially the upper and lower interface sides overlap.

stiffness has to be supplied. We now define the differential operator matrix **L** which is used to relate the continuous element displacement field to the relative displacement vector:

$$\mathbf{L}=\begin{bmatrix} -1 & +1 & 0 & 0 & 0 & 0 \\ 0 & 0 & -1 & +1 & 0 & 0 \\ 0 & 0 & 0 & 0 & -1 & +1 \end{bmatrix} \tag{25}$$

With the interpolation matrix **H**

$$\mathbf{H}=\begin{bmatrix} \mathbf{n}^{\mathrm{T}} & 0 & 0 & 0 & 0 & 0 \\ 0 & \mathbf{n}^{\mathrm{T}} & 0 & 0 & 0 & 0 \\ 0 & 0 & \mathbf{n}^{\mathrm{T}} & 0 & 0 & 0 \\ 0 & 0 & 0 & \mathbf{n}^{\mathrm{T}} & 0 & 0 \\ 0 & 0 & 0 & 0 & \mathbf{n}^{\mathrm{T}} & 0 \\ 0 & 0 & 0 & 0 & 0 & \mathbf{n}^{\mathrm{T}} \end{bmatrix} \tag{26}$$

where **n** is the interpolation polynomial vector and the nodal displacement vector

$$\mathbf{a}^{\mathrm{T}}=(\mathbf{a}_3^1, a_3^2, \ldots, a_3^n, a_2^1, a_2^2, \ldots, a_2^n, a_1^1, a_1^2, \ldots, a_1^n) \tag{27}$$

we can relate the relative displacement vector **v** to the nodal displacements through

$$\mathbf{v}=\mathbf{LHa} \tag{28}$$

If we denote the stiffness matrix of the interface element in the elastic, non-fractured stage by $D_1$, the tractions $t^{\mathrm{T}}=(t_n, t_s, t_t)$ are obtained from

$$\mathbf{t}=D_1\mathbf{v} \tag{29}$$

For a line interface element in a generalised plane-strain situation the element stiffness matrix then reads

$$\mathbf{K}=\int_{\xi=-1}^{\xi=+1} \mathbf{B}^{\mathrm{T}} D_1 \mathbf{B}\, \det\mathbf{J}\, \mathrm{d}\xi \tag{30}$$

in which $\xi$ is the iso-parametric coordinate and $\det \mathbf{J}=[(\partial r_2/\partial\xi)^2+(\partial r_3/\partial\xi)^2]^{1/2}$ is determinant of the Jacobian matrix. The formulation of the element stiffness matrix in a geometrically nonlinear analysis can be found in Refs 16 and 22.

Once the criterion which defines the boundary of the area of elasticity in an integration point of interface element is violated, the traction-relative displacement relation becomes nonlinear. In this contribution an orthotropic softening plasticity model is utilised to describe the mode-I and mixed-mode delamination fracture in composites. Its formulation will be presented in the next section.

## 3 AN ORTHOTROPIC SOFTENING PLASTICITY MODEL

The yield condition for interface plasticity is assumed to be of the form

$$\Phi(\mathbf{t},\kappa)=C_{nn}t_n^2+C_{ss}t_s^2+C_{tt}t_t^2+C_n t_n-\bar{t}^2(\kappa)=0 \tag{31}$$

with $C_{ii}$ and $C_n$ a set of material constants. $t_n$ is the normal traction in the interface and $t_t$ and $t_s$ are the shear tractions. A cross-section of the applied yield surface and the $t_n, t_t$ plane is depicted in Fig. 4. If $\bar{t}_n^c$ and $\bar{t}_n^t$ denote the compressive and tensile yield tractions in the direction normal to the interface plane, and if $\bar{t}_s$ and $\bar{t}_t$ are the shear yield tractions and $\bar{t}$ a normalised yield traction, substitution of these equations in condition (31) results in:

$$C_{nn}=\frac{\bar{t}^2}{\bar{t}_n^t\bar{t}_n^c}\quad C_{ss}=\frac{\bar{t}^2}{\bar{t}_s^2}\quad C_{tt}=\frac{\bar{t}^2}{\bar{t}_t^2}\quad C_n=\frac{\bar{t}^2}{\bar{t}_n^t}-\frac{\bar{t}^2}{\bar{t}_n^c} \tag{32}$$

Recasting eqn (31) in matrix–vector notation yields

$$\Phi(\mathbf{t},\kappa)=\frac{1}{2}\mathbf{t}^T\mathbf{P}\mathbf{t}+\mathbf{t}^T\mathbf{p}-\bar{t}^2(\kappa)=0 \tag{33}$$

in which $\mathbf{t}^T=(t_n,t_s,t_t)$, $\mathbf{P}=\text{diag}\,(2C_{nn},2C_{ss},2C_{tt})$ and $\mathbf{p}^T=(C_n,0,0)$.

As soon as this condition is satisfied, the total relative displacement rate $\dot{\mathbf{v}}$ is decomposed into an 'elastic' part, $\dot{\mathbf{v}}^{el}$, and a 'plastic' part, $\dot{\mathbf{v}}^{pl}$, as follows:

$$\dot{\mathbf{v}}=\dot{\mathbf{v}}^{el}+\dot{\mathbf{v}}^{pl} \tag{34}$$

The elastic relative displacement rate is related to the traction rate by

$$\mathbf{t}=\mathbf{D}_1\dot{\mathbf{v}}^{el} \tag{35}$$

and the assumption of an associated flow rule yield for the plastic relative displacement rate:

$$\dot{\mathbf{v}}^{pl}=\dot{\lambda}\frac{\partial\Phi}{\partial\mathbf{t}} \tag{36}$$

For the present orthotropic yield criterion (33) this gives:

$$\dot{\mathbf{v}}^{pl}=\dot{\lambda}(\mathbf{P}\mathbf{t}+\mathbf{p}) \tag{37}$$

Furthermore, we introduce the scalar $\kappa$ as a measure of the amount of softening. In the case of a work -softening hypothesis $\kappa$ reads

$$\kappa=\int\dot{\kappa}\,dt\quad\text{with}\quad\dot{\kappa}=\mathbf{t}^T\dot{\mathbf{v}}^{pl} \tag{38}$$

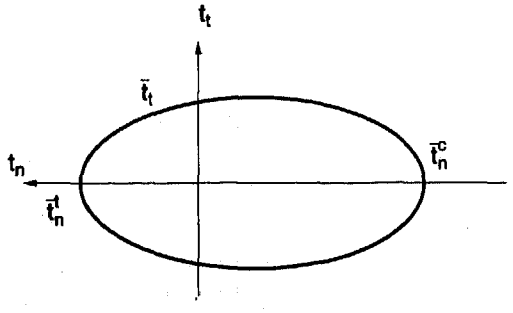


**Fig. 4.** Failure envelope of the orthotropic plasticity model.

### 3.1 Integration of the elasto-plastic relations

A Backward-Euler scheme is used to integrate the rate equations (34)–(38). For finite increments of loading we then obtain:

$$\Delta \mathbf{v}_j = \Delta \mathbf{v}_j^{\mathrm{el}} + \Delta \mathbf{v}_j^{\mathrm{pl}} \tag{39}$$

$$\Delta \mathbf{v}_j^{\mathrm{el}} = \mathbf{D}_{\mathrm{I}}^{-1} \Delta \mathbf{t}_j \tag{40}$$

$$\Delta \mathbf{v}_j^{\mathrm{pl}} = \Delta \lambda_j (\mathbf{P}\mathbf{t}_j + \mathbf{p}) \tag{41}$$

$$\Delta \kappa_j = \mathbf{t}_j^{\mathrm{T}} \Delta \mathbf{v}_j^{\mathrm{pl}} \tag{42}$$

A combination of relations (39)–(41) yields after some rearranging

$$\mathbf{t}_j = (\mathbf{D}_{\mathrm{I}}^{-1} + \Delta \lambda_j \mathbf{P})^{-1} (\mathbf{v}_{i-1}^{\mathrm{el}} + \Delta \mathbf{v}_j - \Delta \lambda_j \mathbf{p}) \tag{43}$$

Subsitution of this expression for $\mathbf{t}_j$ in the yield condition (33) results in a nonlinear equation in $\Delta\lambda_j$: $\Phi(\Delta\lambda_j) = 0$, which can be solved by a local Newton–Raphson procedure:

$$\Delta \lambda_j^{k+1} = \Delta \lambda_j^{k} - \left. \frac{\Phi}{\dfrac{\partial \Phi(\Delta\lambda)}{\partial \Delta \lambda}} \right|_{\Delta \lambda_j^k} \tag{44}$$

The derivative of $\boldsymbol{\Phi}(\Delta\lambda_j)$ with respect to $\Delta\lambda_j$ in eqn (44) reads

$$\frac{\partial \Phi(\Delta\lambda_j)}{\partial \Delta \lambda_j} = \left( \frac{\partial \Phi}{\partial \mathbf{t}_j} \right)^{\mathrm{T}} \frac{\partial \mathbf{t}_j}{\partial \Delta \lambda_j} + \frac{\partial \Phi}{\partial \kappa} \frac{\partial \kappa}{\partial \Delta \boldsymbol{\nu}_j^{pl}} \frac{\partial \Delta \boldsymbol{\nu}_j^{pl}}{\partial \Delta \lambda_j} + \frac{\partial \Phi}{\partial \kappa} \left( \frac{\partial \kappa}{\partial \mathbf{t}_j} \right)^{\mathrm{T}} \frac{\partial \mathbf{t}_j}{\partial \Delta \lambda_j} \tag{45}$$

and can be elaborated to give:

$$\frac{\partial \Phi(\Delta\lambda_j)}{\partial \Delta \lambda_j} = -(\mathbf{P}\mathbf{t}_j + \mathbf{p})^{\mathrm{T}} (\mathbf{D}_{\mathrm{I}}^{-1} + \Delta \lambda_j \mathbf{P})^{-1} ((\mathbf{D}_{\mathrm{I}}^{-1} + \Delta \lambda_j \mathbf{P})^{-1} \mathbf{P} (\mathbf{v}_{i-1}^{\mathrm{el}} + \Delta \mathbf{v}_j - \Delta \lambda_j \mathbf{p}) + \mathbf{p}) - h \tag{46}$$

where

$$h = -\left. \frac{\partial \Phi}{\partial \kappa} \mathbf{t}^{\mathrm{T}} \frac{\partial \Phi}{\partial \mathbf{t}} \right|_{\mathbf{t}_j} \tag{47}$$

is the softening modulus. The softening parameter $\boldsymbol{\kappa}$ is then updated according to

$$\Delta \kappa_j = \Delta \lambda_j \mathbf{t}_j^{\mathrm{T}} (\mathbf{P}\mathbf{t}_j + \mathbf{p}) \tag{48}$$

### 3.2 The consistent tangent operator for orthotropic plasticity

The derivation of the consistent tangent stiffness relation for orthotropic softening plasticity in interface elements is outlined below. Due to the softening type of response, terms occur in the nonlinear equations which eventually result in a non-symmetric tangent stiffness relation.

The total relative displacement vector at the end of iteration $j$ is given by

$$\mathbf{v}_j = \mathbf{v}_{i-1} + \Delta \mathbf{v}_j^{\mathrm{el}} + \Delta \mathbf{v}_j^{\mathrm{pl}} \tag{49}$$

where $\mathbf{v}_{i-1}$ is the relative displacement vector at the beginning of the loading step. With the relations for the incremental elastic and plastic relative displacements

$$\Delta \mathbf{v}_j^{\mathrm{el}} = \mathbf{D}_{\mathrm{I}}^{-1} (\mathbf{t}_j - \mathbf{t}_{i-1}) \tag{50}$$

and

$$\Delta \mathbf{v}_j^{\mathrm{pl}} = \Delta\lambda_j \frac{\partial \Phi}{\partial \mathbf{t}_j} \tag{51}$$

the traction-relative displacement relation can be written as

$$\mathbf{v}_j = \mathbf{v}_{j-1} + \mathbf{D}_{\mathrm{I}}^{-1}(\mathbf{t}_j - \mathbf{t}_{i-1}) + \Delta\lambda_j \frac{\partial \Phi}{\partial \mathbf{t}_j} \tag{52}$$

The time derivative of eqn (52) reads

$$\dot{\mathbf{v}}_j = \mathbf{D}_{\mathrm{I}}^{-1}\dot{\mathbf{t}}_j + \Delta\lambda_j \frac{\partial^2 \Phi}{\partial \mathbf{t}_j^2}\dot{\mathbf{t}}_j + \dot{\lambda}\frac{\partial \Phi}{\partial \mathbf{t}_j} \tag{53}$$

From eqns (42) and (51) we obtain after differentiation

$$\dot{\kappa} = \Delta\lambda_j \left(\frac{\partial \kappa}{\partial \mathbf{v}_j^{\mathrm{pl}}}\right) \frac{\partial^2 \Phi}{\partial \mathbf{v}_j^2}\dot{\mathbf{t}}_j + \dot{\lambda}_j \left(\frac{\partial \kappa}{\partial \mathbf{v}_j^{\mathrm{pl}}}\right) \frac{\partial \Phi}{\partial \mathbf{t}_j} + \left(\frac{\partial \kappa}{\partial \mathbf{t}_j}\right)^{\mathrm{T}} \dot{\mathbf{t}}_j \tag{54}$$

which, upon substitution in the consistency condition

$$\dot{\Phi} = \left(\frac{\partial \Phi}{\partial \mathbf{t}}\right)^{\mathrm{T}} \dot{\mathbf{t}} + \frac{\partial \Phi}{\partial \kappa}\dot{\kappa} = 0 \tag{55}$$

leads to

$$\dot{\Phi} = \left(\frac{\partial \Phi}{\partial \mathbf{t}_j}\right)^{\mathrm{T}} \dot{\mathbf{t}}_j + \Delta\lambda_j \frac{\partial \Phi}{\partial \kappa}\left(\frac{\partial \kappa}{\partial \mathbf{v}_j^{\mathrm{pl}}}\right) \frac{\partial^2 \Phi}{\partial \mathbf{t}_j^2}\dot{\mathbf{t}}_j + \dot{\lambda}_j \frac{\partial \Phi}{\partial \kappa}\left(\frac{\partial \kappa}{\partial \mathbf{v}_j^{\mathrm{pl}}}\right) \frac{\partial \Phi}{\partial \mathbf{t}_j} + \frac{\partial \Phi}{\partial \kappa}\left(\frac{\partial \kappa}{\partial \mathbf{t}_j}\right)^{\mathrm{T}} \dot{\mathbf{t}}_j = 0 \tag{56}$$

Now the time derivative of the plastic multiplier $\dot{\lambda}$ can be solved as

$$\dot{\lambda}_j = \frac{1}{h}\left(\left(\frac{\partial \Phi}{\partial \mathbf{t}_j}\right)^{\mathrm{T}} + \Delta\lambda_j \frac{\partial \Phi}{\partial \kappa}\left(\frac{\partial \kappa}{\partial \mathbf{v}_j^{\mathrm{pl}}}\right) \frac{\partial^2 \Phi}{\partial \mathbf{t}_j^2} + \frac{\partial \Phi}{\partial \kappa}\left(\frac{\partial \kappa}{\partial \mathbf{t}_j}\right)^{\mathrm{T}}\right) \dot{\mathbf{t}}_j \tag{57}$$

in which $h$ is given by eqn (47). Substituting the above expression for $\dot{\lambda}$ into eqn (53) yields the consistently linearised traction-relative displacement relation $\dot{\mathbf{v}}_j$

$$\dot{\mathbf{v}}_j = \left[\mathbf{D}_{\mathrm{I}}^{-1} + \Delta\lambda_j \frac{\partial^2 \Phi}{\partial \mathbf{t}_j^2} + \frac{1}{h}\frac{\partial \Phi}{\partial \mathbf{t}_j}\left(\frac{\partial \Phi}{\partial \mathbf{t}_j}\right)^{\mathrm{T}} + \frac{\Delta\lambda_j}{h}\frac{\partial \Phi}{\partial \kappa}\left(\frac{\partial \Phi}{\partial \mathbf{t}_j}\right)\left(\frac{\partial \kappa}{\partial \mathbf{v}_j^{\mathrm{pl}}}\right)\frac{\partial^2 \Phi}{\partial \mathbf{t}_j^2} + \frac{1}{h}\frac{\partial \Phi}{\partial \kappa}\left(\frac{\partial \Phi}{\partial \mathbf{t}_j}\right)\left(\frac{\partial \kappa}{\partial \mathbf{t}_j}\right)^{\mathrm{T}}\right]\dot{\mathbf{t}}_j \tag{58}$$

At this point a matrix $\mathbf{H}$ is introduced

$$\mathbf{H} = \mathbf{D}_{\mathrm{I}}^{-1} + \Delta\lambda_j \frac{\partial^2 \Phi}{\partial \mathbf{t}_j^2} + \frac{\Delta\lambda_j}{h}\frac{\partial \Phi}{\partial \kappa}\underline{\left(\frac{\partial \Phi}{\partial \mathbf{t}_j}\right)\left(\frac{\partial \kappa}{\partial \mathbf{v}_j^{\mathrm{pl}}}\right)}\frac{\partial^2 \Phi}{\partial \mathbf{t}_j^2} + \frac{1}{h}\frac{\partial \Phi}{\partial \kappa}\left(\frac{\partial \Phi}{\partial \mathbf{t}_j}\right)\left(\frac{\partial \kappa}{\partial \mathbf{t}_j}\right)^{\mathrm{T}} \tag{59}$$

The underlined part in eqn (59) introduces the non-symmetry in the matrix $\mathbf{H}$, which renders the tangential stiffness matrix to be non-symmetric (see eqn (61)). With eqn (59), eqn (58) can conveniently be rewritten as

$$\dot{\mathbf{v}}_j = \left[\mathbf{H} + \frac{1}{h}\frac{\partial \Phi}{\partial \mathbf{t}_j}\left(\frac{\partial \Phi}{\partial \mathbf{t}_j}\right)^{\mathrm{T}}\right]\dot{\mathbf{t}}_j \tag{60}$$

Use of the Sherman–Morrison–Woodbury formula then yields the consistent tangent stiffness relation

$$\dot{\mathbf{t}}_j = \left[ \mathbf{H}^{-1} - \frac{\mathbf{H}^{-1}\left(\frac{\partial \Phi}{\partial \mathbf{t}_j}\right)\left(\frac{\partial \Phi}{\partial \mathbf{t}_j}\right)^{\mathrm{T}}\mathbf{H}^{-1}}{h + \left(\frac{\partial \Phi}{\partial \mathbf{t}_j}\right)^{\mathrm{T}}\mathbf{H}^{-1}\left(\frac{\partial \Phi}{\partial \mathbf{t}_j}\right)} \right] \dot{\mathbf{v}}_j \tag{61}$$

### 3.3 Model aspects

Due to the fact that we intend to model both plasticity and cracking in the interface we can no longer regard the inelastic deformations as being purely plastic. We define the inelastic relative displacements as crack relative displacements ($\mathbf{v}^{cr}$) except for the mode-I inelastic relative displacements that are induced by a compressive loading. These are considered as plastic (see Fig. 5).

The degradation of the elastic properties of the interface is coupled with the inelastic relative displacement due to cracking ($\mathbf{v}^{cr}$). In this case the stiffness that determines the tractions in unloading or reloading is the so-called secant stiffness matrix denoted by $\mathbf{D}_j^s$. From the moment of crack-closure, that is in the compressive loading regime, the initial elastic stiffness governs the interface behaviour. It is assumed that due to the irreversible plastic relative displacements ($v_n^{pl}$) that may occur, the traction relative displacement diagram shifts horizontally over a distance $v_n^{pl}$ (see Fig. 5). Furthermore the assumption is made that the degradation of the equivalent yield traction $\bar{t}$ is not influenced by yielding in compression. Thus the amount of inelastic work that is used to determine $\bar{t}$ and $C_n$ is defined as $\dot{\kappa} = \mathbf{t}^{\mathrm{T}}\dot{\mathbf{v}}^{cr}$. In the computations presented in Sections 4 and 5 we have assumed a linear dependency between the equivalent yield traction $\bar{t}$ and $\kappa$ according to: $\bar{t} = \bar{t}_0(1 - \kappa/G_c)$, with $\bar{t}_0$ and $G_c$ denoting the initial transverse tensile strength and the fracture toughness of the ply interface respectively.

A physical interpretation of the work-softening model is that once the fracture toughness of the interface has been released as free-surface energy, the strength and stiffness of the interface will have completely reduced to zero.

## 4 FINITE ELEMENT COMPUTATIONS

### 4.1 Numerical simulations

We will start the simulations of free edge delamination with the analysis of mode-I delamination in a $[\pm 25/90]_s$ specimen. The results of the experiments are reported by Wang *et al.*[5,11] The mechanical are thermal properties of the AS-3501-06 graphite–epoxy prepreg are collected in Table 1.

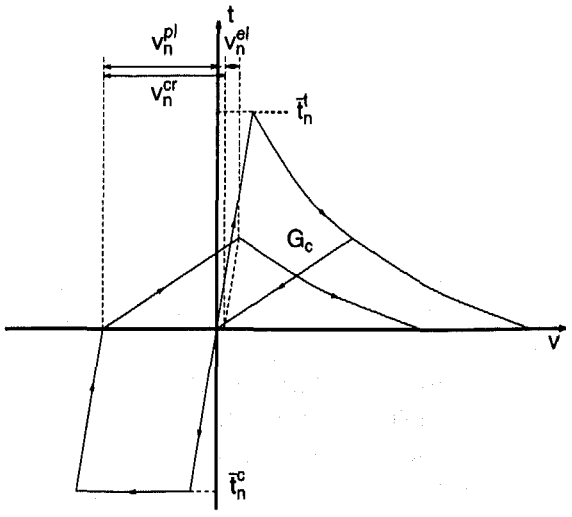


**Fig. 5.** Traction-relative displacement diagram for the normal component ($t_n$ versus $v_n$).

The values for $G_{23}$ and $\nu_{23}$ are assumptions which had to be made owing to a lack of data. In the nonlinear analyses the laminates are exposed to a temperature drop equal to $\Delta T = -125°C$ to account for the residual thermal stresses that are present in the laminate due to the manufacturing process. Also hygroscopic effects can have a significant influence on the laminate strength (cf. Ref. 9). Nevertheless they have not been included in the analyses ($\Delta C = 0$) because of the lack of experimental data.

The total width of the laminates and the thickness of the plies were equal to 25·0 mm and 0·132 mm respectively (Fig. 6). Because of symmetry considerations only a quarter of the cross-section of the specimen was modelled. Cubic twelve-noded generalised plane-strain elements were used to model the individual plies and cubic line interface elements were supplied to connect the

**Table 1. Material properties for AS-3501-06 graphite–epoxy (MPa)**

| Young's moduli | Shear moduli | Poisson ratios | Thermal expansion coefficients |
|---|---|---|---|
| $E_{11}$ $140\times10^{+3}$ | $G_{12}$ $5{\cdot}5\times10^{+3}$ | $\nu_{12}$ 0·29 | $\alpha_{11}$ $0{\cdot}36\times10^{-6}$/°C |
| $E_{22}$ $11\times10^{+3}$ | $G_{13}$ $5{\cdot}5\times10^{+3}$ | $\nu_{13}$ 0·29 | $\alpha_{22}$ $28{\cdot}8\times10^{-6}$/°C |
| $E_{33}$ $11\times10^{+3}$ | $G_{23}$ $5{\cdot}5\times10^{+3}$ | $\nu_{23}$ 0·3 | $\alpha_{33}$ $28{\cdot}8\times10^{-6}$/°C |

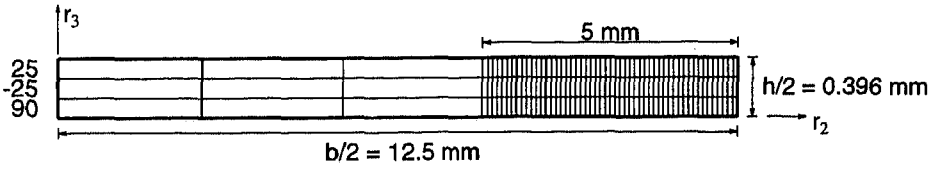


$u_1(0,0,r_3)=0,\quad u_2(0,0,r_3)=0,\quad u_3(0,r_2,0)=0$

**Fig. 6.** Finite element model for a quarter of a cross-section and the associated boundary conditions.

plies. Calculations have shown that cubic elements are well suited to represent the high stress gradients near the free edge. Along the $r_2$-axis of the laminate the nodal translations in the $r_3$-direction were prevented, while translations in the $r_1$- and $r_2$-directions are suppressed along the $r_3$-axis.

The continuum elements were integrated using a $4\times4$ Gauß scheme. For the interface elements four-point Newton–Cotes integration rule was applied, since a Gauß scheme results in spurious oscillations in the stress profiles at locations where high stress gradients exist.[16,25,26] The initial stiffness of the interface elements was chosen equal to $d_i=10^{+8}$ N/mm$^3$ $(i=n,s,t)$. For the transverse tensile strength of graphite–epoxy a value of $\bar{t}_n^t=51{\cdot}6$ N/mm$^2$ was substituted as is given in Ref. 27. In all the nonlinear analyses the post-failure behaviour of the interface elements was determined by a linear softening relation. To achieve a rate-controlled delamination a fracture toughness equal to $G_c=0{\cdot}175$ N/mm has been used.[5,11]

In the mode-I delamination analyses we have investigated the mesh sensitivity of the results. Three different finite element meshes were used with a varying number of elements over the width of the specimen. In all cases the element height was chosen to equal the ply thickness. The part of the specimen within 5 mm of the free edge was modelled using 50, 100 and 200 elements respectively for each ply (element lengths: 0·1, 0·05 and 0·025 mm). The remaining 7·5 mm was modelled using three elements per ply. The nonlinear analyses start with a stepwise decrease in the temperature to −125°C followed by the application of the uniaxial strain load. Figure 7

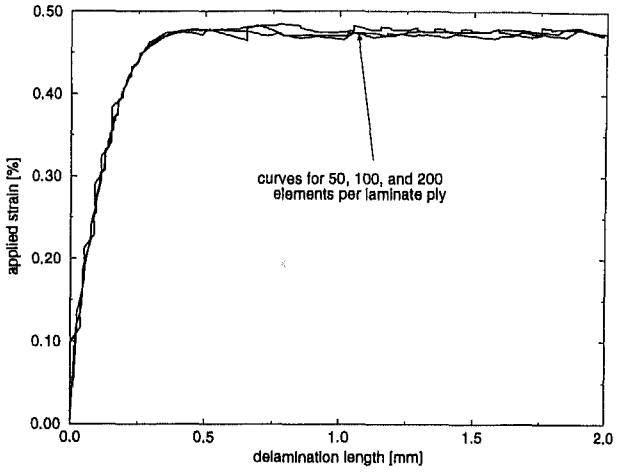


**Fig. 7.** Effects of the element size (element lengths 0·1, 0·05, 0·025 mm) on the numerical results. Ultimate strain versus the length of the delamination crack.

presents the results for the three different meshes. The value obtained for the ultimate uniaxial strain $\varepsilon_u=0{\cdot}48\%$ is in good agreement with the result $\varepsilon_u=0{\cdot}53\%$ that can be derived from data given in Refs 5 and 11. Even more importantly, it is observed that, upon mesh refinement, the different analyses converge to the same solution.

In the mixed-mode delamination analyses fracture was investigated in $[\pm30/\pm30/0/90]_s$ laminates and $[\pm45_n/0_n/90_n]_s$ laminates subjected to tensile loading.[6,7] The material data for the T300-5208 epoxy prepreg are listed in Table 2. The values for the tensile, compressive and shear strengths are taken from Ref. 27.

The analysis of these mixed-mode specimens is somewhat different from the mode-I analyses,

**Table 2. Material properties for T300-5208 graphite–epoxy (MPa)**

| Young's moduli | Shear moduli | Poisson ratios | Yield strengths |
|---|---|---|---|
| $E_{11}$ $138\times10^{+3}$ | $G_{12}$ $5{\cdot}9\times10^{+3}$ | $\nu_{12}$ 0·21 | $\bar{t}_n^t$ 40·0 |
| $E_{22}$ $15\times10^{+3}$ | $G_{13}$ $5{\cdot}9\times10^{+3}$ | $\nu_{13}$ 0·21 | $\bar{t}_n^c$ 246·0 |
| $E_{33}$ $15\times10^{+3}$ | $G_{23}$ $5{\cdot}9\times10^{+3}$ | $\nu_{23}$ 0·21 | $\bar{t}_s, \bar{t}_t$ 68·0 |

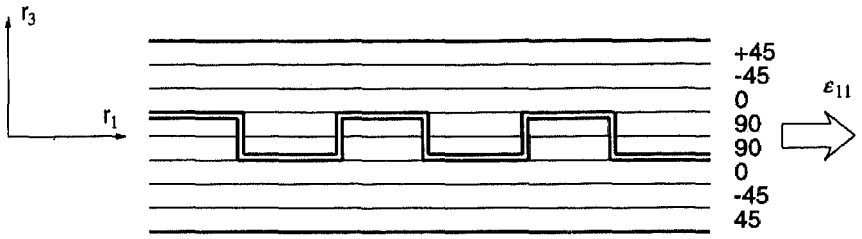


**Fig. 8.** Schematic representation of the jumping of a delamination crack between an interface and its symmetric counterpart.

since the temperature drop that was imposed to create the internal thermal stress field is now omitted. This is because in the fracture toughness value of these laminates as determined by O'Brien,[6] the effect of the initial thermal stresses is implicitly included. Another important issue is that the value for the critical energy release rate $G_c = 0{\cdot}137$ N/mm as derived by O'Brien, corresponds to a single delamination along the free edge which 'jumps' between the two 0/90 interfaces as depicted in Fig. 8 (see Ref. 6). Therefore the value for $G_c$ that is substituted in the fracture model should be equal to $G_c = 0{\cdot}0685$ N/mm since we assume mirror-symmetry about the $r_2$-axis.

The results of a mesh refinement study are presented in Fig. 9. The element length was again varied between 0·025 and 0·1 mm. A laminate with a stacking sequence equal to $[\pm45/0/90]_s$ was selected.[7] The ply thickness and the specimen width for the mixed-mode specimens were respectively 0·15 mm and 38·0 mm. It is observed that also in the mixed-mode analyses the results converge to a unique solution. In Fig. 10 the influence of mesh-refinement on the energy release rate per mode is presented. We observe that during delamination growth the energy released in each mode is not constant. However, similar to the strain curves, the energy curves are almost identical for the three different meshes. Hence, mesh-insensitivity has been achieved for the energy release rates per fracture mode. Since the mode-II energy release rates were not significant they have been omitted from Fig. 10.

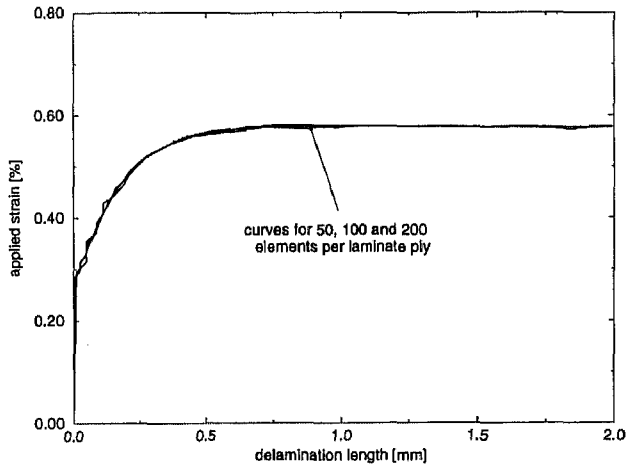


**Fig. 9.** Effects of the element size (element lengths 0·1, 0·05, 0·025 mm) on the numerical results. Ultimate strain versus the length of the delamination crack.

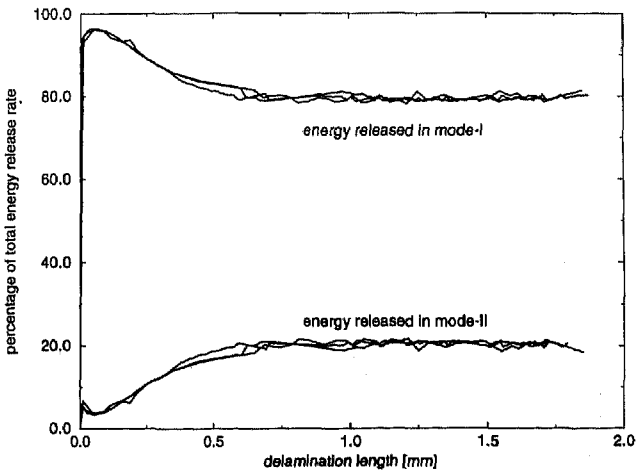


**Fig. 10.** The effects of mesh refinement on the energy release rate per mode.

Finally Figs 11a and 11b show the effect of the laminate thickness on the ultimate tensile strain for these laminates. The element length in these analysis was equal to 0·1 mm. Similar to the mode-I analyses reported in Ref. 22 the results demonstrate an inverse dependency of the ultimate strain on the laminate thickness. The agreement between numerical and experimental results appears to be reasonable, as can be observed from Fig. 11b (cf. Refs 6 and 7).

### 4.2 Numerical predictions

Although the numerical simulations of the mixed-mode delamination experiments reported in the literature indicate that the predictive value of the applied finite element approach is good, it was decided to carry out a limited experimental study to obtain additional data for the verification of the mixed-mode model.

Before starting the experiments, numerical calculations on several laminates with varying stacking sequences have been performed in order to find a stacking sequence which would most probably result in mixed-mode delamination. Based on these analyses it was decided to use a $[0/\pm 35/90]_s$ stacking sequence. The material that has been used to manufacture the specimens is a Fibredux 6376C/35/135/HTA (resin content $35 \pm 2{\cdot}5\%$) increased toughness graphite–epoxy prepreg of which the properties are collected in Table 3.

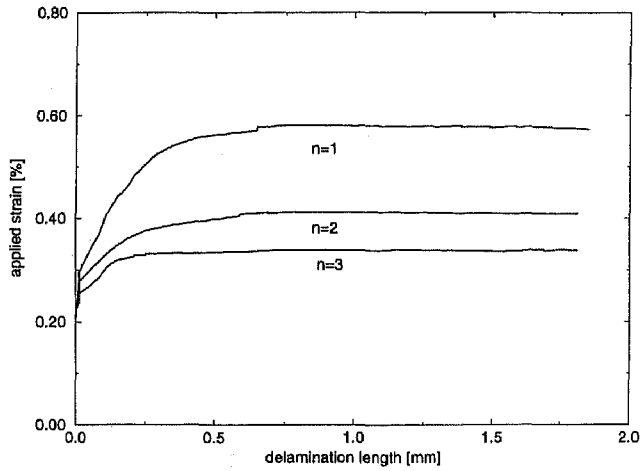


**Fig. 11a.** Applied uniaxial strain versus delamination length for different numbers of plies (8, 16 and 24).

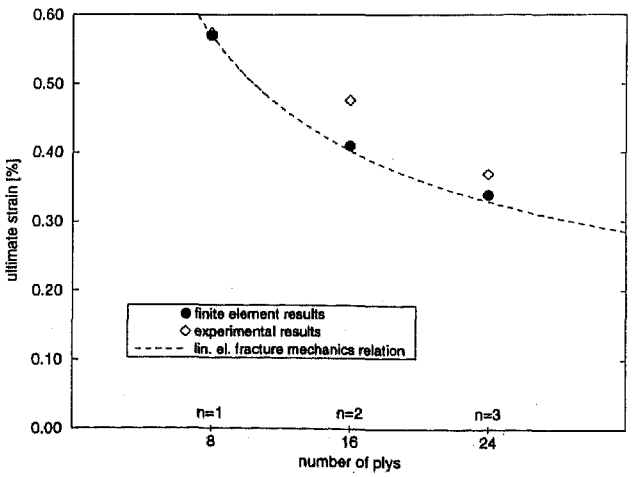


**Fig. 11b.** Ultimate strain versus laminate thickness.

The fracture toughness values of the material were: $G_{Ic} = 0{\cdot}310$ N/mm and $G_{IIc} = 0{\cdot}750$ N/mm. During delamination growth the ratio between $G_I$ and $G_{II}$ was calculated to be 0·27/0·73. Therefore, for the mixed-mode fracture toughness a value of $0{\cdot}27 \times 0{\cdot}310 + 0{\cdot}73 \times 0{\cdot}75 = 0{\cdot}631$ N/mm was substituted. The width of the specimen and the ply-thickness were taken equal to 25·0 mm and 0·125 mm respectively. Numerical predictions were made of the delamination onset strain and location of the delamination crack. The analyses started with a stepwise decrease in the temperature to $-150{\cdot}0$°C followed by the strain loading. For the thermal expansion coefficients the values of Table 1 were substituted since they were not given on the material suppliers data sheets. In the calculations the effect of the laminate thickness on the ultimate strain was determined. The results are presented in Fig. 12.

In the analyses a single delamination crack was assumed, jumping between two symmetric ply interfaces as was observed by O'Brien.[6] The plot of the deformed model in Fig. 13 demonstrates that the delamination crack occurs in the $-35/90$ interface. The delamination crack that is shown in the figure has a length of approximately 2·0 mm.

## 5 MIXED-MODE EDGE DELAMINATION EXPERIMENTS

In order to verify the predictive capabilities of the constitutive model that has been developed for the description of delamination onset and growth, mixed-mode delamination experiments have been performed at the facilities of the Department of Metallurgy and Applied Materials Science of the Katholieke University Leuven.

The laminates that were used in the experiments were fabricated from Fibredux increased toughness graphite–epoxy prepregs (see previous section) and autoclaved at 175°C according to the recommendations provided by the supplier. The dimensions of the test specimens that were cut

**Table 3. Material properties for 6376C/35/135/HTA graphite-epoxy (MPa)**

| Young's moduli | Shear moduli | Poisson ratios | Yield strengths |
|---|---|---|---|
| $E_{11}$ $140\times10^{+3}$ | $G_{12}$ $5{\cdot}8\times10^{+3}$ | $\nu_{12}$ 0·21 | $\bar{t}_n^t$ 70·0 |
| $E_{22}$ $9{\cdot}5\times10^{+3}$ | $G_{13}$ $5{\cdot}8\times10^{+3}$ | $\nu_{13}$ 0·29 | $\bar{t}_n^c$ 240·0 |
| $E_{33}$ $9{\cdot}5\times10^{+3}$ | $G_{23}$ $5{\cdot}8\times10^{+3}$ | $\nu_{23}$ 0·29 | $\bar{t}_s, \bar{t}_t$ 105·0 |

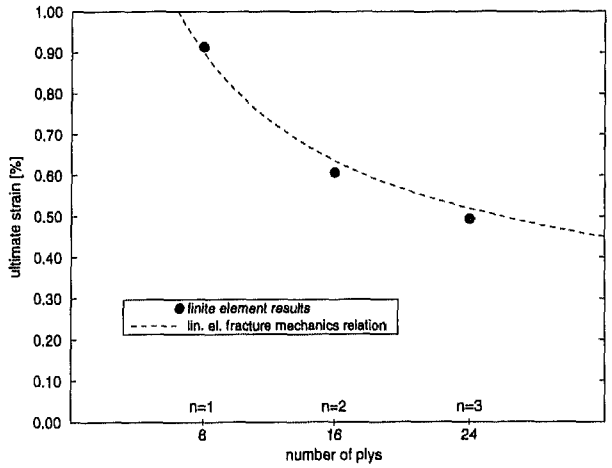


**Fig. 12.** Numerical predictions of the failure strain of $[0_n/\pm35_n/90_n]_s$ laminates ($n=1,2,3$) showing the existence of the size effect.

from the laminated plates were: length 240·0 mm and width 25·0 mm. The cured ply thickness was equal to approximately 0·118 mm. To assess the quality of the prepreg plates from which the delamination specimens were cut the ultrasonic C-Scan technique has been applied. For the installation in the testing machine and to achieve a proper load transfer end tabs with a length of 40·0 mm were attached to the strips. Three different thicknesses were selected for the $[0_n/\pm35_n/90_n]_s$ specimens in order to identify the size effects in the fracture process ($n=1$, 2 and 3). For each laminate thickness a series of five or six specimens was fabricated in order to check the reproducibility of the results.

In the experiments the laminates were subjected to uniaxial tensile loading in an Instron 6025 testing device at a controlled cross-head speed of 0·25 mm/min. The uniaxial strain in the laminates was recorded using an extensometer which had glued to the specimens. The occurrence of matrix cracks and the onset of delamination was triggered by acoustic emission techniques.

During the tests it was observed that prior to delamination onset matrix cracks occurred in the 90° layers with a regular spacing. The crack pattern appeared to have a saturation distance approximately equal to the thickness of the 90° layer as could be observed from X-radiographs.[16]

Subsequent to the occurrence of the matrix cracks an edge delamination started at the 35/90 interface and jumped through the cracks over to the symmetric counterpart (see Figs 14 and 15). Further in the loading process occasionally a delamination crack appeared in the 35/−35 interface and in the 90° layer. The load level at which the matrix cracks and delamination cracks occurred decreased with increasing laminate thickness. Furthermore the difference in load level at delamination onset and at the start of matrix cracking decreased with the laminate thickness.

The average values of the experimental results are collected in Table 4 in terms of delamination onset stresses and strains. In Fig. 16 the comparison is made between numerical predictions and the experimental values and we see that there is a good correspondence between them. This observation still holds if we account for the difference in actual and modelled ply-thickness (0·118 mm and 0·125 mm respectively) and consequently as a result of the thickness effect the values of the calculated strains increase with ±3%. Furthermore from Fig. 16 it is observed that for all three laminate thicknesses the experimental scatter is limited.

## 6 CONCLUDING REMARKS

In view of the results presented in this contribution it is concluded that the present calculation strategy for the analysis of mode-I and mixed-mode free edge delamination does not suffer from spurious influences of mesh refinement on the delamination growth. This is a result of the inclusion of the fracture toughness in the constitutive relations for the interface elements which yields a softening type of response after the onset of delamination. The agreement with experimental results and numerical simulations is good. Furthe-

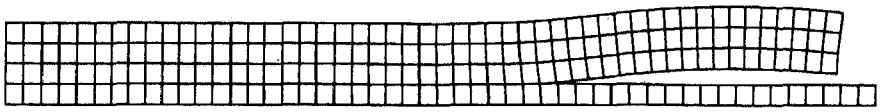

Fig. 13. Deformed model with a crack length of 2·0 mm ($r_2$–$r_3$ plane).

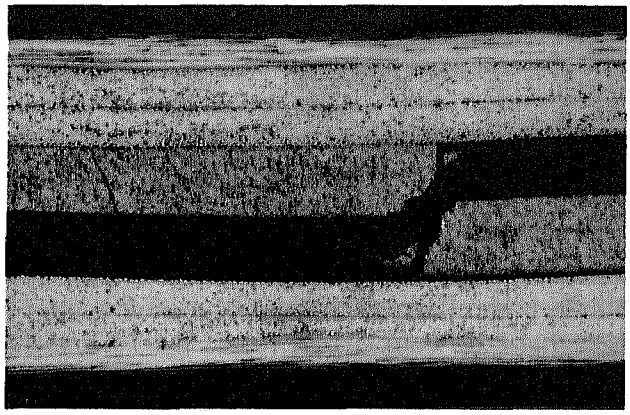

Fig. 14. Edge delamination in a $[0/\pm 35/90]_s$ laminate, view of the free edge ($r_1$–$r_3$ plane).

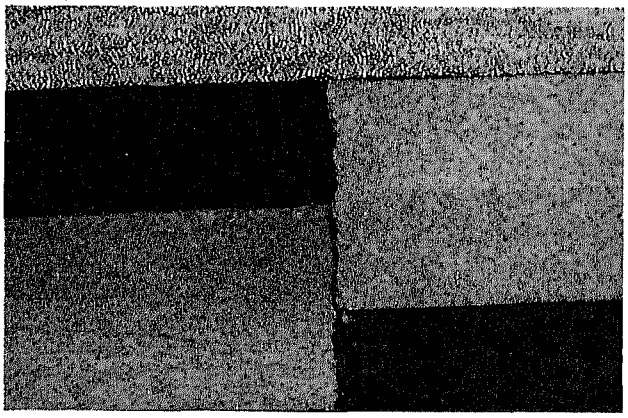

Fig. 15. Edge delamination in a $[0/\pm 35/90]_s$ laminate. Close-up of the jumping of the delamination crack between the $-35/90$ interfaces ($r_1$–$r_3$ plane).

Table 4. Experimental results for $[0_n/\pm 35_n/90_n]_s$ laminates

| $n$ | $E_{11}$ (N/mm$^2$) | $\varepsilon_{11}$ | $\bar{\sigma}_{11}$ (N/mm$^2$) |
|---|---|---|---|
| 1 | 65014·0 | 0·912 | 581·0 |
| 2 | 66421·0 | 0·622 | 427·0 |
| 3 | 68095·0 | 0·522 | 344·0 |

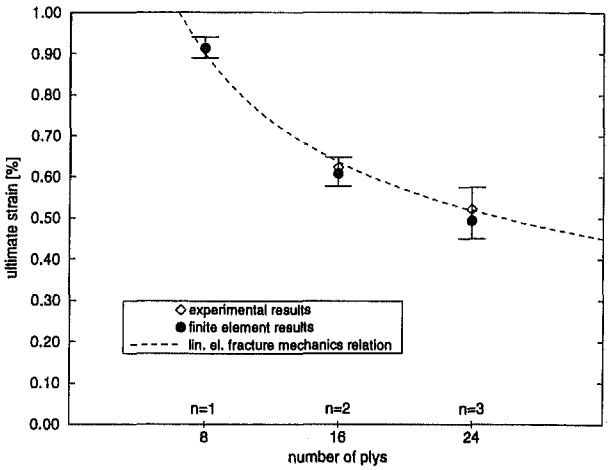


Fig. 16. Comparison of finite element predictions and experimental results. The ultimate strain as a function of the laminate thickness.

more the approach results in a proper treatment of size effects.

## ACKNOWLEDGEMENTS

We would like to express our gratitude to Professor I. Verpoest of the Department of Metallurgy and Materials Engineering of the Katholieke Universiteit Leuven for making his experimental facilities available. Also the assistance of his coworkers J. Ivens and P. Rubbrecht during the implementation of the experiments, is highly appreciated. The calculations carried out in this paper have been carried out using a pilot version of the DIANA finite element programme of TNO Building and Construction Research.

## REFERENCES

1. Pipes, R. B. & Pagano, N. J., Interlaminar stresses in composite laminates under uniform axial extension. *J. Comp. Mater.*, **4** (1970) 538–44.
2. Pagano, N. J., On the calculation of interlaminar normal stress in composite laminates. *J. Comp. Mater.*, **8** (1974) 65–81.
3. Crossman, F. W. & Wang, A. S. D., The dependence of transverse cracking and delamination on ply thickness in graphite/epoxy laminates. In *Damage in Composite Materials*, ed. K. L. Reifsnider. ASTM STP 775, ASTM, Philadelphia, PA, 1982, pp. 118–39.
4. Kim, R. Y. & Soni, S. R., Experimental and analytical studies on the onset of delamination in laminated composites. *J. Comp. Mater.*, **18** (1984) 70–6.

5. Wang, A. S. D., Slomiana, M. & Bucinell, R. B., Delamination crack growth in composite laminates. In *Delamination and Debonding of Materials*, ed. W. S. Johnson. ASTM STP 876, ASTM, Philadelphia, PA, 1985, pp. 135–67.
6. O'Brien, T. K., Characterisation of delamination onset and growth in a composite laminate. In *Damage in Composite Materials*, ed. K. L. Reifsnider. ASTM STP 775, ASTM, Philadelphia, PA, 1982, pp. 140–67.
7. O'Brien, T. K., Mixed-mode strain-energy-release rate effects on edge delamination of composites. In *Effects of Defects in Composite Materials*. ASTM STP 836, ASTM, Philadelphia, PA, 1984, pp. 125–42.
8. O'Brien, T. K., Analysis of local delaminations and their influence on composite laminate behaviour. In *Delamination and Debonding of Materials*, ed. W. S. Johnson. ASTM STP 876, ASTM, Philadelphia, PA, 1985, pp. 282–97.
9. O'Brien, T. K., Raju, I. S. & Garber, D. P., Residual thermal and moisture influences on the strain energy release rate analysis of edge delamination. *J. Comp. Technol. Res.*, **8** (2) (1986) 37–47.
10. Pagano, N. J. & Soni, S. R., Models for studying free-edge effects. In *Interlaminar Response of Composite Materials*, ed. N. J. Pagano, Elsevier, Amsterdam, 1989, pp. 1–68.
11. Wang, A. S. D., Fracture analysis of interlaminar cracking. *Interlaminar Response of Composite Materials*, ed. N. J. Pagano. Elsevier Science Publishers B.V., Amsterdam, 1989, pp. 69–109.
12. Deaudeville, L., Une méthode simplifée pour l'analyse du délaminage des structures composites stratifiées. Dissertation, Université Paris VI, ENS Cachan, Cachan, 1992.
13. Tsai, S. W. & Wu, E. M., A general theory of strength for anisotropic materials. *J. Comp. Mater.*, **5** (1971) 58–80.
14. Pijaudier-Cabot, G. & Bazant, Z. P., Nonlocal damage theory. *ASCE J. Engng Mech.*, **113** (1987) 1512–33.
15. Schellekens, J. C. J. & Borst, R. De, Application of linear and nonlinear fracture mechanics options to free edge delamination in laminate composites. *HERON*, **36** (2) (1991) 37–48.
16. Schellekens, J. C. J., Computational strategies for composite structure. Dissertation, Delft University of Technology, Delft, 1992.
17. Schellekens, J. C. J. & Borst, R. De, Application of anisotropic softening plasticity to mixed-mode delamination in composites. *Proc. Third Int. Conf. on Comp. Plast.*, ed. D. R. J. Owen, E. Oñate & E. Hinton. Pineridge Press, Swansea, 1992, pp. 1671–83.
18. Riks, E., On the numerical solution of snapping problems in the theory of elastic stability. Dissertation, Stanford University, Stanford, 1970.
19. Crisfield, M. A., A fast incremental/iterative solution procedure that handles snap-through. *Comp. Struct.*, **13** (1/3) (1981) 55–62.
20. Ramm, E., Strategies for tracing the nonlinear response near limit points. In *Nonlinear Finite Element Analysis in Structural Mechanics*, ed. W. Wunderlich *et al.* Springer Verlag, Berlin, 1981, pp. 63–89.
21. Borst, R. De, Computation of post-bifurcation and post-failure behaviour of strain-softening solids. *Comput. Struct.*, **25** (1987) 211–24.
22. Schellekens, J. C. J. & Borst, R. De, A non-linear finite element approach for the analysis of mode-I free edge delamination in composites. *Int. J. Solids Struct.*, **30** (9) (1993) 1239–53.
23. Schellekens, J. C. J. & Borst, R. De, Nonlinear analysis of propagation of delamination near free edges. *Proc. Int. Conf. Comp. Materials*, ed. S. W. Tsai & G. S. Springer. SAMPE, Covina, California, 1991, Paper E-28.
24. Schellekens, J. C. J. & Borst, R. De, Simulation of free edge delamination via finite element techniques. In *New Advances in Computational Structural Mechanics*, ed. P. Ladeveze & O. C. Zienkiewicz. Elsevier Science Publishers B.V., Amsterdam, 1992, pp. 397–410.
25. Schellekens, J. C. J. & Borst, R. De, On the integration of interface elements. *Int. J. Num. Meth. Engng*, **36** (1993) 43–66.
26. Rots, J. G., Computation modelling of concrete fracture. Dissertation, Delft University of Technology, Delft, 1988.
27. Tsai, S. W., *Composites Design*. Think Composites, Dayton, Ohio, 1988.